

Electronic Supplementary Information (ESI)

Thermodynamics and defect chemistry of substitutional and interstitial doping in layered α -V₂O₅.

Kit McColl^a, Ian Johnson^a and Furio Corà^{*a}

^a Christopher Ingold Building, Department of Chemistry, University College London, 20 Gordon Street, London, WC1H 0AJ, UK.

Corresponding author:

*Furio Corà.

E-mail: f.cora@ucl.ac.uk

Tel: +44 207 6797482

Table of contents

1. Atomistic simulation methods	2
2. Density functional theory methods	5
3. DFT dispersion interactions	6
4. Determination of reaction energies	7
5. Pair potential vs. QM techniques	13
6. Ion migration energy calculations	15
7. Supplementary references	15

1. Atomistic simulation methods.

Atomistic simulations to investigate the reaction energetics for substitutional and interstitial cations in α -V₂O₅ were conducted using empirically-fitted pair-potential methods. These methods are well established for the investigation of dopants in battery cathode materials, and their details are discussed extensively elsewhere.^{1,2} Here we give a summary of the methods used. All calculations were performed with the General Utility Lattice Program (GULP).³ All systems are described as ionic crystalline solids, and ion-ion interactions are described by a combination of long-range Coulombic and short-range interactions. Short-range interactions are described by two potentials. The majority are Buckingham potentials (Table S1), of the form:

$$\phi_{ij}(r_{ij}) = A_{ij} \exp\left(\frac{-r_{ij}}{\rho_{ij}}\right) - \left(\frac{C_{ij}}{r^6}\right) \quad 1)$$

where r is the inter-ion distance, A , ρ and C are constants and i and j are indices of the interacting ions. To reproduce the layered structure of V₂O₅, one short-range Morse potential is used, between the V and O1 atoms of the vanadyl group (Table S2), of the form:

$$\phi_{ij}(r_{ij}) = D_0 \left(\{1 - \exp[\alpha(r - r_0)]\}^2 - 1 \right) \quad 2)$$

where D_0 , α and r_0 are constants. The Morse potential reproduces the short V-O_{1_{vanadyl}} bond, whilst a Buckingham potential with a minimum distance of 1.99 Å reproduces the V-O1 interlayer distance (i.e. between a V and the O1 that it is not bound to through a vanadyl bond). The remaining equatorial bonds are generated with V-O and O-O Buckingham potentials. This model has previously been used successfully to represent the structure and properties of V₂O₅.⁴ The other ion-ion interactions are described by potentials that have been used to investigate a range of transition metal oxides in a consistent manner.⁵ All the potentials used are listed in Tables S1 and S2 below. Ion polarizability is described using the shell model of Dick and Overhauser,⁶ and the parameters used are shown in Table S3. Defect calculations, including migration profiles are implemented using the Mott-Littleton scheme using region I and region II sizes of 10.0 and 25.0 Å respectively.⁷

i) Pair potentials

Table S1. Buckingham potentials and cutoffs.

Interaction	A / eV	ρ / Å	C / eV Å ⁶	r_{\min} / Å	r_{\max} / Å
V ⁵⁺ -O _{2,O3}	5312.99	0.26797	0.0	0.0	10.0
V ⁵⁺ ...O _{1interlayer}	2549.73	0.34115	0.0	1.99	10.0
V ⁴⁺ -O	1260.56	0.34039	0.0	0.0	10.0
O-O	22764.30	0.1490	23.0	0.0	10.0
Na ⁺ -O	1271.504	0.300	0.0	0.0	10.0
Li ⁺ -O	426.480	0.300	0.0	0.0	10.0
K ⁺ -O	3587.570	0.300	0.0	0.0	10.0
Ag ⁺ -O	962.197	0.300	0.0	0.0	10.0
Cu ⁺ -O	585.747	0.300	0.0	0.0	10.0
Pb ⁺ -O	5564.374	0.2610	0.0	0.0	10.0
Rb ⁺ -O	2565.507	0.3260	0.0	0.0	10.0
Mg ²⁺ -O	2457.243	0.2610	0.0	0.0	10.0
Ca ²⁺ -O	2272.741	0.2986	0.0	0.0	10.0
Ba ²⁺ -O	4818.416	0.3067	0.0	0.0	10.0
Fe ²⁺ -O	2763.945	0.2641	0.0	0.0	10.0
Sr ²⁺ -O	1956.702	0.3252	0.0	0.0	10.0
Al ³⁺ -O	2409.505	0.2649	0.0	0.0	10.0
Ag ³⁺ -O	4534.200	0.2649	0.0	0.0	10.0
Eu ³⁺ -O	847.868	0.3791	0.0	0.0	10.0
Fe ³⁺ -O	3219.335	0.2641	0.0	0.0	10.0
Ga ³⁺ -O	2339.776	0.2742	0.0	0.0	10.0
Gd ³⁺ -O	866.339	0.3770	0.0	0.0	10.0
La ³⁺ -O	5436.827	0.2939	0.0	0.0	10.0
Tb ³⁺ -O	845.137	0.3750	0.0	0.0	10.0
Y ³⁺ -O	1519.279	0.3291	0.0	0.0	10.0
Yb ³⁺ -O	991.029	0.3515	0.0	0.0	10.0
Ti ⁴⁺ -O	4545.823	0.2610	0.0	0.0	10.0
Sn ⁴⁺ -O	6327.497	0.2610	0.0	0.0	10.0
Ce ⁴⁺ -O	2409.505	0.3260	0.0	0.0	10.0
Mn ⁴⁺ -O	3329.388	0.2642	0.0	0.0	10.0
Ge ⁴⁺ -O	3703.725	0.2610	0.0	0.0	10.0
Zr ⁴⁺ -O	7290.347	0.2610	0.0	0.0	10.0

Table S2. Morse potential parameters and cutoff.

Interaction	D ₀ / eV	α / Å ⁻¹	r ₀ / Å	r _{min} / Å	r _{max} / Å
V ⁵⁺ -O _{1vanadyl}	10.0	2.302170	1.584	0.0	1.99

Table S3. Core-shell model parameters and spring constants.

Species	$q_{\text{core}} / e $	$q_{\text{shell}} / e $	$k / \text{eV \AA}^2$
V ⁵⁺	5.0	-	-
V ⁴⁺	4.0	-	-
O ²⁻	0.717	-2.717	54.952
Na ⁺	1.0	-	-
Li ⁺	1.0	-	-
K ⁺	1.0	-	-
Ag ⁺	1.0	-	-
Cu ⁺	1.0	-	-
Pb ⁺	1.0	-	-
Rb ⁺	1.0	-	-
Mg ²⁺	1.58	0.42	349.95
Ca ²⁺	0.719	1.281	34.05
Ba ²⁺	0.169	1.831	34.05
Fe ²⁺	2.0	-	-
Sr ²⁺	0.169	1.831	21.53
Al ³⁺	0.043	2.957	403.98
Ag ³⁺	3.0	-	-
Eu ³⁺	-0.991	3.991	304.92
Fe ³⁺	1.971	1.029	179.58
Ga ³⁺	3.0	-	-
Gd ³⁺	-0.973	3.973	299.96
La ³⁺	5.149	-2.149	173.90
Tb ³⁺	-0.972	3.972	299.98
Y ³⁺	3.0	-	-
Yb ³⁺	-0.278	3.278	308.91
Ti ⁴⁺	4.0	-	-
Sn ⁴⁺	4.0	-	-
Ce ⁴⁺	4.0	-	-
Mn ⁴⁺	4.0	-	-
Ge ⁴⁺	4.0	-	-
Zr ⁴⁺	4.0	-	-

2. Density functional theory calculations.

First-principles calculations were performed using the periodic density functional theory (DFT) code CRYSTAL17.^{8,9} Electronic exchange and correlation were approximated using the hybrid-exchange functional B3LYP,¹⁰ which is known to give accurate estimates of the band structure of crystalline solids.¹¹ All-electron atom-centred Gaussian basis sets were used for all atoms, available from the CRYSTAL online database (www.crystal.unito.it), indicated by the following labels online: V (V_86-411d31G_harrison_1993), O (O_8-411d1_cora_2005), Al (Al_86-21G*_harrison_1993) and Fe (Fe_s86411p6411d411_Heifets_2013). The Coulomb and exchange series were truncated with thresholds of 10^{-7} , 10^{-7} , 10^{-7} , 10^{-7} and 10^{-14} . Reciprocal space was sampled using a Pack-Monkhorst net,¹² with a shrinking factor of $IS = 8$ along each periodic direction. The self-consistent field (SCF) procedure was performed up to a convergence threshold of $\Delta E = 10^{-8}$ Hartree per unit cell. Full geometry optimisations (lattice parameters and atomic positions) were performed using the default convergence criteria in CRYSTAL17. The interactions between layers in V_2O_5 are predominantly of a Van-der Waals type, and therefore dispersion effects are important in accurately describing the structure.¹³ The inclusion of dispersion forces is discussed in greater detail in Section 3. Excluding the tests where the functional is explicitly identified, all the DFT calculations carried out in the paper use Grimme's empirical D3 correction to B3LYP (B3LYP-D3).¹⁴ Defect calculations were performed using the supercell method, and the expansion of the crystallographic unit cell is indicated in the text for each case.

3. DFT dispersion interactions.

The interlayer forces in α -V₂O₅ contain an important contribution from van der Waals (vdW) type interactions and a good representation of dispersion forces is therefore important in accurately describing the structure of α -V₂O₅. Previous theoretical work on V₂O₅ has often included the effects of dispersion through vdW-formulated functionals,^{13,15} although some studies on ionic mobility in V₂O₅ have omitted these effects, citing increased insertion energies for ions and increased diffusion barriers.¹⁶ The failure of functionals that do not include dispersion effects to reproduce the correct structure of layered V₂O₅ is clear from the lattice parameters of α -V₂O₅ calculated using B3LYP, which result in an over-estimation of the interlayer c-axis by 13.2% against the experimental value (Table S4 - ICSD collection code 60767).¹⁷ An improvement is made using the D2 dispersion correction scheme proposed by Grimme,¹⁸ reducing the error to an expansion of 3.5%. The most recent parameterisation, the D3 scheme,¹⁴ produces a further improvement, and gives an overestimation of the c-direction by +0.2%, which is in good agreement with experiment. The a and b parameters are also well reproduced, as are the interatomic distances (Table S5), demonstrating that B3LYP-D3 gives an excellent structural description of α -V₂O₅.

Method	a / Å	b / Å	c / Å	Vol / Å ³
Expt. ¹⁷	11.510	3.563	4.369	179.173
B3LYP-D3	11.490 (-0.2%)	3.544 (-0.5%)	4.378 (+0.2%)	178.272 (-0.5%)
B3LYP-D2	11.512 (+0.0%)	3.536 (-0.8%)	4.521 (+3.5%)	184.042 (+2.7%)
B3LYP	11.448 (-0.5%)	3.582 (+0.5%)	4.944 (+13.2%)	202.787 (+13.2%)

Table S4. Lattice constant of α -V₂O₅ calculated using DFT with different levels of dispersion theory. Numbers in parentheses indicate the difference with respect to the experimental value.

Interatomic distance	Expt. ¹⁷	B3LYP-D3	B3LYP-D2	B3LYP
V-O1 / Å	1.581	1.577 (-0.3%)	1.577 (-0.3%)	1.575 (-0.4%)
V-O2 / Å	1.780	1.776 (-0.2%)	1.779 (-0.1%)	1.787 (+0.4%)
V-O3 / Å	1.881	1.877 (-0.2%)	1.879 (-0.1%)	1.896 (+0.8%)
V-O3' / Å	2.022	2.031 (+0.4%)	2.048 (+1.3%)	2.026 (+0.2%)
V-O1(interlayer) / Å	2.793	2.801 (+0.3%)	2.940 (+5.3%)	3.122 (11.8%)

Table S5. Interatomic distances in α -V₂O₅ calculated using DFT with different levels of dispersion theory. Numbers in parentheses indicate the difference with respect to the experimental value.

4. Determination of reaction energies.

i) Stability of isolated oxygen-ion vacancies.

Oxygen-ion vacancies play an important role in defect equilibria in V_2O_5 . They are present as intrinsic defects to balance for V^{4+} , but can also be generated extrinsically to balance changes in charge introduced by cation dopants. The energies of oxygen-ion vacancies are therefore required to determine the overall reaction energies of different dopant ion defects. Isolated intrinsic oxygen-ion vacancies can occur at three possible symmetry inequivalent sites in the crystallographic unit cell; O1 (vanadyl oxygen), O2 and O3 (Figure 1, main text). In the pair-potential calculations, the vanadyl group (VO^{3+}) is treated as a single tightly bound unit. Breaking the $V-O1_{\text{vanadyl}}$ bond described by the Morse potential results in an O-vacancy energy that is inconsistent with the removal of O-ions whose interatomic forces are modelled only by Buckingham and Coulomb potentials. We have therefore used the energy of an O2 vacancy (26.65 eV) to calculate reaction energies in the following section, when the energy of an isolated oxygen-ion vacancy is required.

Oxygen-ion vacancy site	Defect energy / eV
O2	26.65
O3	30.47

Table S6. Isolated intrinsic oxygen-ion vacancy energies calculated in GULP.

ii) Geometry of clustered dopant and oxygen-ion defects.

Substitutional M^{n+} ions ($n < 5$) can be charge compensated by oxygen-ion vacancies. Due to the electrostatic interactions between the negatively charged $M_V^{(5-n)^-}$ defect and positively charged oxygen-ion vacancy sites, the most stable arrangement may be as a defect cluster rather than as isolated vacancies. We have therefore considered reaction equations that include all relevant combinations of isolated and clustered defects, to assess which is the most stable incorporation scheme for substitutional M^{n+} ($n < 5$) ions. For clustered defects, we have assessed the stability of oxygen vacancies at each of the symmetry inequivalent O-sites relative to the dopant, as indicated in Figure S1.

Introduction of a substitutional dopant breaks the symmetry of the structure, increasing the number of symmetry unique O-ions in the first coordination shell that can be removed to form a clustered vacancy. Relative to the dopant, there are two inequivalent O1 atoms, denoted $O1_{\text{vanadyl}}$ and $O1_{\text{interlayer}}$ and two inequivalent O3 atoms, denoted O3 and O3'. Interatomic distances are indicated in Table S5. $O1_{\text{interlayer}}$ vacancies undergo rearrangement

to a geometry that is equivalent to the removal of $O1_{\text{vanadyl}}$, and have the same energy as $O1_{\text{vanadyl}}$ vacancies, therefore we have included only the energies of clustered $O1_{\text{vanadyl}}$ vacancies for O1 sites.

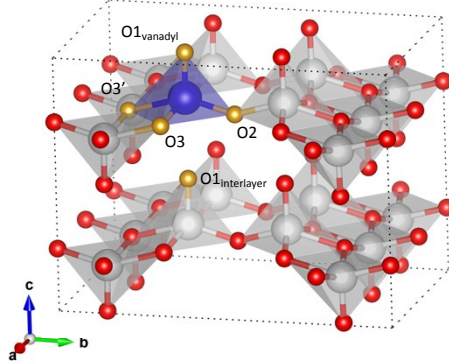
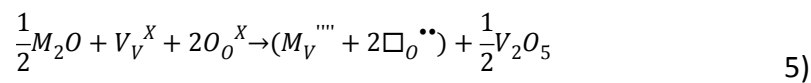
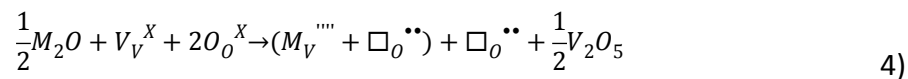
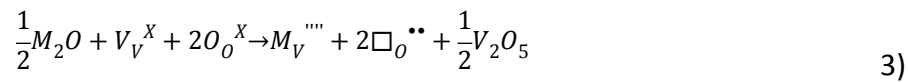


Figure S1. Position of oxygen vacancy sites for a substitutional M^{n+} dopant. V atoms are grey, O atoms are red. The blue sphere indicates the substitutional M^{n+} cation, and gold spheres indicate the oxygen vacancy positions

iii) Evaluating stable configurations for substitutional M^{n+} ions.

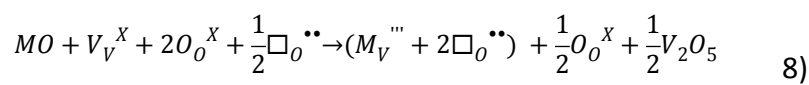
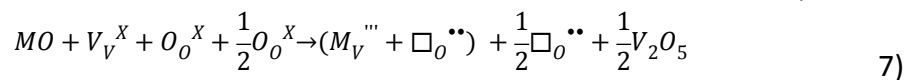
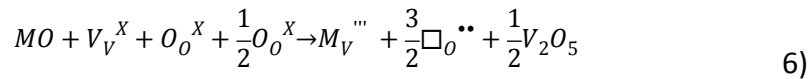
M^+ defects are compensated by two oxygen-ion vacancies to form a neutral overall defect. We consider these situations; the first, isolated defects (Equation 3), the second a clustered cation with one oxygen-ion vacancy and a 2nd oxygen-ion vacancy as an isolated defect (Eq. 4), and the third a cluster of two oxygen-ion vacancies around the substituting cation (Eq. 5). The defects that form clusters in adjacent sites are indicated in brackets:



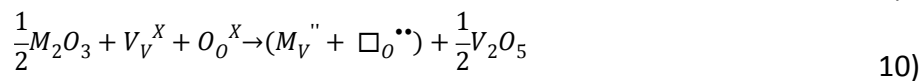
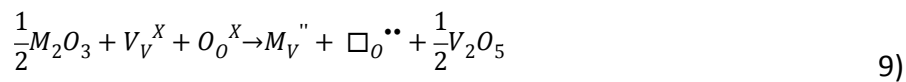
For all ions studied, the situation where two oxygen-ion vacancies are clustered with the substitutional M^+ ion (Eq. 5) is the most stable. In this defect cluster we find the most stable configuration is for oxygen-ion vacancies to be at the vanadyl O1 and O3 sites relative to the substituted cation (Figure S1). Calculated energies of substitutional M^+ dopants are summarised in Table S7.

M^{2+} defects require the compensation of 1.5 oxygen-ion vacancies per substituting cation (or 3 oxygen-ion vacancies per 2 cations). We calculated the energies of the isolated (Eq. 6), clustered defects with one cation and one oxygen-ion vacancy (giving an overall charge of -1,

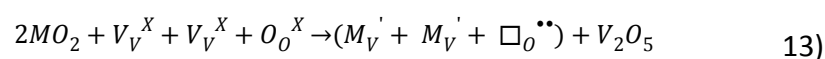
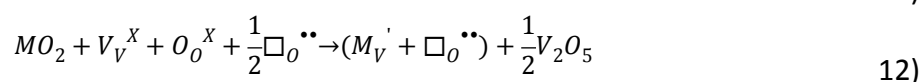
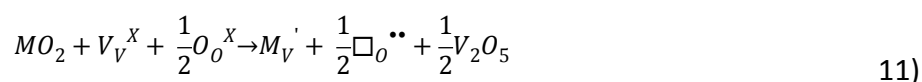
Eq. 7) and one cation and two oxygen-ion vacancies (giving an overall charge of +1, Eq. 8). In the case of the single oxygen-ion vacancy, the most stable site was at the vanadyl O1 site. In the case of the double oxygen ion vacancy, the most stable configuration, as with the M⁺ defects, was at the vanadyl O1 and O3 sites. The double oxygen-ion vacancy cluster (Eq. 8) was found to be the lowest energy structure. Calculated energies of substitutional M²⁺ dopants are summarised in Table S8.



M³⁺ defects are compensated by a single oxygen-ion vacancy to form a neutral overall defect. The defects can either be isolated (Eq. 9) or clustered (Eq. 10). For all dopants, a clustered defect was found to be more stable than isolated defects, and the most stable site for the oxygen-ion vacancy was at the vanadyl O1 site relative to the substituting M³⁺ ion. Calculated energies of substitutional M³⁺ dopants are summarised in Table S9.

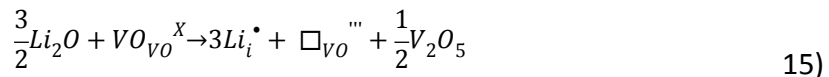
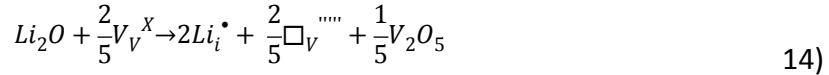


M⁴⁺ ions can be incorporated to form an isolated M_v' defect, with each dopant compensated by 0.5 oxygen-ion vacancies (Eq. 11). Alternatively, a clustered defect with an oxygen vacancy adjacent to the dopant site can form, with an overall charge of +1 (Eq. 12). A neutral clustered defect could be formed by a single oxygen-ion defect per two cations (Eq. 13). We investigated these possible configurations, and found the most stable defect to be a positively charged cluster (Eq. 14), with the oxygen-ion vacancy at the O1 site. Calculated energies of substitutional M⁴⁺ dopants are summarised in Table S10.



iv) Interstitial dopants.

Interstitial cations introducing a positive charge can be charge compensated by four possible mechanisms that introduce negative charge. The following reaction equations are given as an example for Li^+ ions. Charge compensation may be via vanadium vacancies (Eq. 14), or $(\text{VO})^{3+}$ vacancies (Eq. 15), interstitial oxide ions (Eq. 16) or or by the reduction of vanadium to V^{4+} , and the loss of oxygen (Eq. 17):



The reaction energies of equations 14, 15 and 16 can be calculated directly using the pair potential methods. The reaction energy of Eq. 17 can be estimated using a combination of experimental and theoretical data:

$$\Delta E = E(\text{Li}_2\text{O}) - EA_1(\text{O}) - EA_2(\text{O}) - 2I_5(\text{V}) + 2E(\text{Li}_i^{\bullet}) + 2E(\text{V}_V^{\prime}) - \frac{1}{2}DE(\text{O}_{2(g)}) \quad 18)$$

Where $EA_1(\text{O})$ and $EA_2(\text{O})$ are the 1st and 2nd electron affinities of O respectively (-1.47 eV and +8.75 eV), $I_5(\text{V})$ is the 5th ionisation energy of V (65.28 eV), $E(\text{Li}_i^{\bullet})$ is the reaction energy of interstitial Li^+ (-8.29 eV), and $DE(\text{O}_{2(g)})$ is the dissociation energy of an oxygen molecule (5.16 eV).

The reaction energy of a reduced V^{4+} site $E(\text{V}_V^{\prime})$, is poorly reproduced by the pair-potential calculations due to breaking of the Morse potential. However, a reliable value can be estimated from the insertion energy of $\text{Li}_{(s)}$ into V_2O_5 :



which has an experimental value of $\Delta E = -3.4$ eV.

$$\Delta E = E_s(\text{Li}_{(s)}) + I_1(\text{Li}) - I_5(\text{V}) + E(\text{Li}_i^{\bullet}) + E(\text{V}_V^{\prime}) \quad 20)$$

Where $E_s(\text{Li}_{(s)})$ is the sublimation energy of Li (1.65 eV) and $I_1(\text{Li})$ is the first ionisation energy of Li (5.39 eV). The reaction energy of V_V^{\prime} is found to be 63.14 eV.

Using these results, we find that cation incorporation compensated by interstitial oxide ions is always stable relative to incorporation compensated by the reduction of vanadium to V^{4+} . Furthermore, interstitial M^{n+} dopants, accompanied by V^{5+} or $(VO)^{3+}$ vacancies for charge balance (Equations 14 & 15) were found to be highly unstable relative to Equations 16 & 17, for all cations. The stable charge compensation scheme for interstitial dopant incorporation was therefore found to be by interstitial oxygen-ions, and the relevant reaction equations are indicated in the main paper (Eq. i), iii), v) and vii)). In these calculations, we are considering a system in which the vanadium is fully oxidised, however synthesis of V_2O_5 generally produces an oxygen-deficient product. The implications of introducing interstitial oxide ions to an oxygen-deficient structure are discussed in the main text.

v) Substitutional defect energies

For the clustered defects, the location of the oxygen-ion vacancies relative to the dopant are indicated at the top of the table. All energies are in eV. The most stable defects are indicated in bold.

Dopant	Eq. 3	Eq. 4				Eq. 5				
		O1	O2	O3	O3'	O1+O2	O1+O3	O1+O3'	O2+O3	O2+O3'
Ag ⁺	18.73	8.74	9.59	11.98	15.10	2.38	6.52	6.92	8.79	7.80
Cu ⁺	25.42	8.83	10.36	14.04	15.81	2.75	6.39	6.45	8.69	8.11
K ⁺	20.90	11.52	11.78	14.16	16.07	3.66	6.51	8.36	8.14	9.84
Li ⁺	18.10	9.21	11.15	15.55	15.09	3.43	6.74	6.72	9.25	8.78
Na ⁺	19.35	9.70	10.40	12.68	15.41	2.84	5.47	7.49	9.21	13.86
Pb ⁺	19.20	9.68	9.84	12.13	14.41	2.13	4.57	6.94	8.79	8.89
Rb ⁺	20.32	12.17	12.45	14.88	16.85	4.36	7.03	8.93	10.73	10.37

Table S7. Calculated reaction energies for substitutional M^+ dopants according to Equations 3 – 5.

Dopant	Eq. 6	Eq. 7				Eq. 8				
		O1	O2	O3	O3'	O1+O2	O1+O3	O1+O3'	O2+O3	O2+O3'
Ba	17.17	6.63	7.53	8.79	11.73	0.41	1.78	2.88	7.39	5.06
Ca	15.35	5.01	5.87	9.80	10.50	-0.44	2.13	2.44	2.91	2.44
Fe	15.97	4.59	6.52	10.45	11.36	-0.17	2.73	2.64	3.64	4.93
Mg	16.36	4.68	6.94	11.59	11.76	0.22	3.01	2.75	4.07	6.29
Sr	15.86	5.53	6.56	9.12	10.73	-0.27	2.13	2.40	3.34	4.20

Table S8. Calculated reaction energies for substitutional M^{2+} dopants according to Equations 6 – 8.

Dopant	Eq. 9	Eq. 10			
		O1	O2	O3	O3'
Al ³⁺	8.06	0.66	2.68	6.55	8.72
Ag ³⁺	6.23	-1.18	0.84	4.72	6.88
Eu ³⁺	6.03	-1.37	0.65	4.52	6.69
Fe ³⁺	7.46	0.05	2.07	5.95	8.11
Ga ³⁺	7.32	-0.08	1.94	5.81	7.97
Gd ³⁺	6.19	-1.22	0.80	4.68	6.84
La ³⁺	6.12	-1.28	0.74	4.61	6.77
Tb ³⁺	5.89	-1.52	0.50	4.38	6.54
Y ³⁺	6.82	-0.58	1.44	5.31	7.48
Yb ³⁺	6.23	-1.17	0.85	4.73	6.89

Table S9. Calculated reaction energies for substitutional M³⁺ dopants according to Equations 9 & 10.

Dopant	Eq. 11	Eq. 12				Eq. 13
		O1	O2	O3	O3'	
Ti ⁴⁺	5.17	1.67	2.69	4.71	9.37	6.61
Sn ⁴⁺	3.80	0.85	2.14	2.74	5.31	6.20
Ce ⁴⁺	3.55	0.49	2.58	4.57	3.48	6.96
Mn ⁴⁺	6.09	3.15	3.25	1.25	4.14	7.23
Ge ⁴⁺	6.01	2.35	3.22	5.20	8.13	7.25
Zr ⁴⁺	4.50	1.55	3.65	5.72	12.30	10.03

Table S10. Calculated reaction energies for substitutional M⁴⁺ dopants according to Equations 11 – 13.

vi) **Interstitial defect energies**

Dopant	Reaction energy / eV
Ag ⁺	-4.74
Cu ⁺	-4.20
K ⁺	-2.86
Li ⁺	-3.31
Na ⁺	-4.13
Pb ⁺	-5.02
Rb ⁺	-1.65
Ba ²⁺	-3.62
Ca ²⁺	-4.78
Fe ²⁺	-3.63

Mg ²⁺	-2.94
Sr ²⁺	-4.48
Al ³⁺	3.53
Ag ³⁺	-1.45
Eu ³⁺	-2.87
Fe ³⁺	0.03
Ga ³⁺	0.43
Gd ³⁺	-2.52
La ³⁺	-3.42
Tb ³⁺	-2.67
Y ³⁺	-2.54
Yb ³⁺	-2.10
Ti ⁴⁺	5.55
Sn ⁴⁺	2.54
Ce ⁴⁺	1.39
Mn ⁴⁺	7.55
Ge ⁴⁺	8.54
Zr ⁴⁺	3.25

Table S11. Calculated reaction energies for interstitial Mⁿ⁺ dopants according to Equations i), iii), v) and vii) in the main text.

5. Pair potential vs. quantum mechanical techniques

A consistent result found from the calculations using pair-potential methods is that upon substitutional Mⁿ⁺ incorporation, oxygen vacancies forming as clustered defects adjacent to the dopant are more stable than isolated defects. Furthermore the most stable site for the oxygen-ion vacancy is always at the vanadyl O1 site, or includes the O1 and another O site if two O-vacancies form a cluster. In some cases, when the oxygen-ion vacancy has been initially created at an O2, O3 or O3' site, we observed a structural rearrangement of oxygen-ion coordination around the substitutional cation to be equivalent in form and energy to a O1 vacancy. This behaviour indicates the preference for the V-O1 unit in the V₂O₅ lattice to behave as a vanadyl-like (VO³⁺) ion upon substitutional doping, rather than as individual V⁵⁺ and O²⁻ ions. The pair potential calculations indicate that this mechanism is more energetically favourable in all cases compared to the substitution of an Mⁿ⁺ ion into a V⁵⁺ site with isolated oxygen vacancies forming elsewhere to compensate charge. The small size of V⁵⁺ ($r = 0.54 \text{ \AA}$) means that the pyramidal coordination for a substitutional cation in V₂O₅ is relatively compressed (Table S5). The loss of the O1 oxygen upon substitution relieves local steric pressure and allows for a larger space into which the substitutional Mⁿ⁺ ion can relax. The vanadyl-ion scheme therefore presents a chemically reasonable substitutional pathway.

Here and in the main text we denote a V-O1 vanadyl-like ion as VO in Kröger-Vink notation. For example:



describes the substitution of a M^{3+} ion into a (VO^{3+}) ion site, resulting in an overall charge neutral defect.

To evaluate the reliability of the clustered defect calculations in GULP, we have compared the results with quantum-mechanical calculations. We have considered the case of the substitutional M^{3+} dopants, Eq. 10. The overall defect is charge neutral, and the results can therefore be directly compared in a periodic calculation between pair-potential and DFT techniques. Al^{3+} ($r = 0.49 \text{ \AA}$) and Fe^{3+} ($r = 0.60 \text{ \AA}$) ions were chosen as example M^{3+} dopants. As well as being 3+ ions and giving charge neutral defects per equation S21, both dopants have ionic radii that put them close to the ‘crossover’ point between greatest stability between interstitial and substitutional 3+ ions. They are therefore candidates for either substitutional or interstitial doping via thermodynamic or kinetic control of reaction conditions. Furthermore, both systems have been examined previously in the literature, and are therefore known to affect the electrochemical properties of V_2O_5 .^{19,20} The energies of substitutional Al^{3+} and Fe^{3+} defects were calculated in CRYSTAL and GULP, using a 2x1x2 (16 cation) supercell, according to the following equation, and the energies are reported in Table S12:

$$\Delta E = E(AlV_{15}O_{39}) - 7.5 E(V_2O_5) - 0.5 E(Al_2O_3) \quad (22)$$

Location for the O-ion vacancy relative to the M_V'' site	Reaction energies / eV			
	Al^{3+}		Fe^{3+}	
	DFT	GULP	DFT	GULP
O1 (vanadyl)	0.99	0.87	0.52	0.58
O2	4.65	2.57	*	5.14
O3	3.49	6.75	*	9.29
O3'	5.06	7.31	2.98	8.64
O1 (interlayer)	1.12	*	0.65	*

Table S12. Reaction energy of clustered $(M_V'' + \square_O^{\bullet\bullet})$ defects ($M = Al^{3+}, Fe^{3+}$) with the O-vacancy at different sites relative to the dopant, calculated using DFT and pair-potentials. The asterisk (*) indicates that a re-arrangement has taken place during the geometry optimisation and the structure relaxes to the same geometry as the O1 defect with an identical reaction energy.

Both the DFT and pair-potential supercell calculations determine O1 to be the stable site for an oxygen-ion vacancy, which is consistent with the Mott-Littleton defect calculations of Section 5 (above). The O2 and O3 vacancies are unstable for Fe³⁺ substitution, calculated using DFT, and the structure undergoes re-arrangement such that the O-vacancy is at the O1 site. The same behaviour is seen for the pair-potential calculated O1_{interlayer} sites. Both the absolute reaction energies and the energy ordering between the configurations calculated using DFT are generally well reproduced by the pair potential calculations, which gives confidence in the reliability of those results. The agreement is particularly good between the reaction energies of the stable O1_{vanadyl} vacancy structures for Al³⁺ and Fe³⁺ using pair-potential and DFT techniques, and thus the DFT results validate the stability of the clustered dopant-O vacancy defects at the vanadyl site obtained with the pair potential calculations.

6. Ion migration energy profiles.

Migration profiles were calculated using the Mott-Littleton method. Ion diffusion was modelled by the stepwise displacement of the Li⁺ or Mg²⁺ ion along the [100] direction. At each point along the pathway, a constrained geometry optimisation was performed, fixing the x-coordinate of the diffusing ion, whilst allowing the y and z coordinates to relax. All other ions in region I were fully relaxed. Dopant ions were introduced in an adjacent interstice relative to the diffusing ion as indicated in Figure 3 (main text) to determine their influence on the migration energy.

The nature of the Mott-Littleton calculations means that they are simulating an isolated defect at infinite dilution. The results for the ion migration are therefore relevant to the initial stages of Li⁺ or Mg²⁺ insertion into the structure only. Furthermore, the migration profiles are known to be affected by the phase of V₂O₅.²¹ At x = 1 in MV₂O₅, where M = Li, Mg, the δ phase of V₂O₅ is observed. However, the pair potentials used here are fitted to reproduce the structure of α-V₂O₅, meaning questions regarding mobility in the δ phase are beyond the scope of this work.

7. Supplementary references

1. Islam, M. S. & Fisher, C. A. J. Lithium and sodium battery cathode materials: computational insights into voltage, diffusion and nanostructural properties. *Chem. Soc. Rev.* **43**, 185–204 (2014).
2. Catlow, C. R. A. *Computer Modelling in Inorganic Crystallography*. (Academic Press, 1997).
3. Gale, J. D. & Rohl, A. L. The General Utility Lattice Program (GULP). *Mol. Simul.* **29**, 291–341 (2003).

4. Braithwaite, J. S., Catlow, C. R. A., Gale, J. D. & Harding, J. H. Lithium Intercalation into Vanadium Pentoxide : a Theoretical Study. *Chem. Mater.* **11**, 1990–1998 (1999).
5. Bush, T. S., Gale, J. D., Catlow, C. R. a. & Battle, P. D. Self-consistent interatomic potentials for the simulation of binary and ternary oxides. *J. Mater. Chem.* **4**, 831 (1994).
6. Dick, B. G. & Overhauser, A. W. Theory of the Dielectric Constants of Alkali Halide Crystals. *Phys. Rev.* **112**, 90–103 (1958).
7. Littleton, N. F. & Mott, M. J. Conduction in Polar Crystals. I. Electrytic Conduction in Solid Salts. *Trans. Faraday Soc* 485–499 (1938).
8. R. Dovesi, V. R. Saunders, C. Roetti, R. Orlando, C. M. Zicovich-Wilson, F. Pascale, B. Civalleri, K. Doll, N. M. Harrison, I. J. Bush, P. D'Arco, M. Llunell, M. Causà, Y. Noël, L. Maschio, A. Erba, M. R. and S. C. CRYSTAL17 User's Manual. University of Torino, Torino. *CRYSTAL17* (2017).
9. Erba, A., Baima, J., Bush, I., Orlando, R. & Dovesi, R. Large-Scale Condensed Matter DFT Simulations : Performance and Capabilities of the CRYSTAL Code. *J. Chem. Theory Comput.* **13**, 5019–5027 (2017).
10. Stephens, P. J., Devlin, F. J., Chabalowski, C. F. & Frisch, M. J. Ab Initio Calculation of Vibrational Absorption and Circular Dichroism Spectra Using Density Functional Force Fields. *J. Phys. Chem.* **98**, 11623–11627 (1994).
11. Corà, F. *et al.* The Performance of Hybrid Density Functionals in Solid State Chemistry. *Struct. Bond.* **113**, 171–232 (2004).
12. Monkhorst, H. J. & Pack, J. D. Special points for Brillouin-zone integrations. *Phys. Rev. B* **13**, 5188–5192 (1976).
13. Carrasco, J. Role of van der Waals forces in thermodynamics and kinetics of layered transition metal oxide electrodes: Alkali and alkaline-earth ion insertion into V2O5. *J. Phys. Chem. C* **118**, 19599–19607 (2014).
14. Grimme, S., Antony, J., Ehrlich, S. & Krieg, H. A consistent and accurate ab initio parametrization of density functional dispersion correction (DFT-D) for the 94 elements H-Pu. *J. Chem. Phys.* **132**, 0–19 (2010).
15. Riffet, V., Contreras-Garclá, J., Carrasco, J. & Calatayud, M. Alkali Ion Incorporation into V2O5: A Noncovalent Interactions Analysis. *J. Phys. Chem. C* **120**, 4259–4265 (2016).
16. Parija, A. *et al.* Topochemically De-Intercalated Phases of V2O5 as Cathode Materials for Multivalent Intercalation Batteries: A First-Principles Evaluation. *Chem. Mater.* **28**, 5611–5620 (2016).
17. Enjalbert, R. & Galy, J. A refinement of the structure of V2O5. *Acta Crystallogr.* **C42**, 1467–1469 (1986).
18. Grimme, S. Semiempirical GGA-Type Density Functional Constructed with a Long-Range Dispersion Correction. *J. Comput. Chem.* **27**, 1787–1799 (2006).
19. Cheah, Y. L., Aravindan, V. & Madhavi, S. Improved Elevated Temperature Performance of Al-Intercalated V2O5 Electrospun Nanofibers for Lithium-Ion Batteries. *ACS Appl. Mater. Interfaces* **4**, 3270–3277 (2012).
20. Liang, X., Gao, G., Liu, Y., Zhang, T. & Wu, G. Synthesis and characterization of Fe-doped vanadium oxide nanorods and their electrochemical performance. *J. Alloys Compd.* **715**, 374–383 (2017).
21. Gautam, G. S. *et al.* First-principles evaluation of multi-valent cation insertion into orthorhombic V2O5. *Chem. Commun.* **51**, 13619–13622 (2015).